Mechanistic analysis from molecular-dynamics simulations: keV-particle-induced desorption from Si{001}

D. E. Sanders,* K. B. S. Prasad, J. S. Burnham, and B. J. Garrison
Department of Chemistry, The Pennsylvania State University, University Park, Pennsylvania 16802
(Received 7 February 1994)

We have developed a method for interpreting and classifying mechanisms from molecular-dynamics simulations. The reason for this effort is that molecular-dynamics simulations contain a wealth of information regarding the microscopic details of atomic motions. It is at best tedious, however, to extract all of the essential information in very complex processes. In particular, we are interested in particle ejection due to the keV-particle bombardment. Our method isolates the motion of the last two collisions, which we depict in a single frame showing the time sequence of the positions of the three atoms involved. The remainder of the atoms are shown at their initial positions. These atoms give the perspective of the entire system but small or irrelevant displacements do not distract from the key motions. This method is utilized to elucidate the structure-sensitive mechanisms of keV-particle bombardment of the {001} face of diamond-lattice crystals. We have observed that two mechanisms are responsible for the major features of the angular distributions, namely, the Δ_1 and the Δ_3 mechanisms. The two mechanisms are characterized by the difference in the number of layers of the atoms involved in the final momentum transfer.

INTRODUCTION

Molecular-dynamics (MD) simulations have been shown to be a powerful technique for modeling keV-particle bombardment of solids.[1] In this process a collision cascade develops within the solid in which atoms and molecules undergo large displacements from their initial configurations. Some of the particles eject into the vacuum and can be detected experimentally. The beauty of the classical mechanics approach for describing this process is that the atomic motions are understandable on an intuitive basis once they are determined. The challenge, though, is that in order to model properly the collision events, several thousand collision cascades need to be calculated, each involving a few thousand atoms. The information is available for understanding all nuclear motion, but the extraction of all the mechanistic information is difficult and tedious. Over the years a number of approaches have been tested including the use of movies and videos,[2-6] several key frames of a movie sequence,[7-9] and one frame into which all action is compressed.[10-13] Each of these approaches has strengths and can be useful, but all these pictorial representations are painfully slow to create and analyze.

The advent of faster computers and more sophisticated graphics packages reopens the question of whether it is possible to analyze a large number of individual collision cascades. In particular, we are interested in the energy and angular distributions of particles that are ejected from solids due to keV-particle bombardment. Although prior analyses were able to determine the dominant atomic motions that give rise to peaks in the distributions, it was not possible to trace all the motions.[14-25] An attempt was made to extract all the essential mechanisms, but it is very difficult to determine if, in fact, this has been accomplished.

The work presented here focuses on the {001} face of the diamond lattice because at present we have experimental data of the energy and angular distributions of particles ejected from several Al adsorbate overlayers on GaAs {001}(2×4), which we desire to understand.[26] It is clear that the angular distributions reflect structural arrangements of atoms but, even with concomitant MD simulations, the relationship between atomic structure and features in the angular distributions cannot be extracted without a detailed analysis of the atomic motions. Another reason for choosing the diamond lattice vs a close-packed metal surface is because initial investigations indicate that the openness of the lattice limits the variety of atomic collisions that are important for ejection.[15,16,18,21,22] The four reconstructions shown in Fig. 1, the (1×1), (2×1), (1×4), and (2×4), are utilized because there is a systematic variation in surface geometry that may impact the collision dynamics in an equally systematic fashion. The dimerized (2×1) surface is observed experimentally for Si{001} (Ref. 27) and the (2×4) geometry is observed for GaAs{001}.[28-31] The clean undimerized (1×1) and (1×4) surfaces are not observed experimentally but can be synthesized for the purpose of our calculations. By studying each reconstruction element separately, we hope to address the effects of surface morphology on the observable distributions in a systematic way. This system provides the initial challenge for the method of analysis of mechanisms.

In the following sections we describe the MD calculations of the keV-particle bombardment of the various reconstructions of the diamond-lattice {001} surfaces. We then present our method for interpreting and classifying mechanisms from the simulations. This method isolates the motion of the last two collisions, which we depict in a single frame showing the time sequence of the positions of the three atoms involved. Finally, this

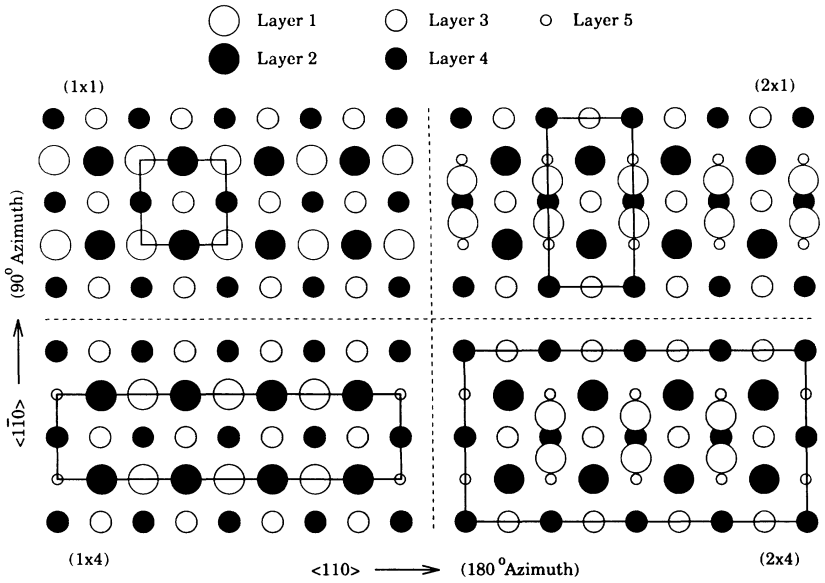

FIG. 1. Four reconstructions of the diamond-lattice {001} surface. Clockwise from top left: (1×1), (2×1), (2×4), and (1×4). The ⟨110⟩ direction has been designated as the 180° azimuth in the text and the ⟨1$\bar{1}$0⟩ direction as 90°. The boxes designate the surface unit cells.

graphical method is used to analyze all the collision events that give rise to ejection of atoms. We find that two basic mechanisms dominate. Both the graphical method of analyzing the important collisional processes and the analysis of the dominant mechanisms of ejection for these four surface reconstructions form the basis of future studies to determine the structures of Al overlayers on GaAs{001} surfaces.[26]

DETAILS OF CALCULATIONS

The computational procedure has been presented elsewhere[15,32,33] and the interested reader is referred there for a detailed explanation of how the MD calculations are performed. Briefly, classical dynamics in the form of Hamilton's equations of motion is used to propagate the positions and velocities of atoms in a solid crystal subsequent to bombardment by a 1-keV Ar atom. The interaction potential for the substrate Si atoms is a many-body form due to Tersoff[34] that was modified[15] to incorporate a more repulsive interaction at short range, and the Ar-Si interaction is the same as used previously. In all cases the initial direction of the Ar atom is normal to the surface plane and the initial aiming points are chosen to uniformly sample the irreducible symmetry subregion of the unit cell. Each trajectory is integrated until the total (kinetic+potential) energy of each atom remaining in the crystal falls below a specified threshold value, at which time it is deemed that no further particles can eject into the vacuum. The final state of atoms that pass through a plane parallel to and above the surface is retained for further analysis.

The crystal sizes for the simulations presented here are 11 layers deep with 154 atoms per layer for the (1×1) surface and 10 layers deep with 224 atoms per layer for the (2×1), (1×4), and (2×4) surfaces. The top layers of the (1×4) and (2×4) surfaces have only 168 atoms each because of the missing-row reconstruction. Portions of each crystal with the unit cells outlined are illustrated in Fig. 1. The equilibrium atom positions for the (2×1) and (2×4) surfaces were determined by a molecular-dynamics simulation with periodic boundary conditions in the two horizontal directions. The bulk-terminated positions were used for the (1×1) and (1×4) surfaces, since any relaxation of these surfaces would result in a dimerized reconstruction. Of note is that the time scale of the simulation is sufficiently short such that the atoms do not relax before the integration is terminated. At the beginning of each Ar-atom impact (i.e., each trajectory) the velocities of the crystal atoms are initialized to zero to approximate a 0-K crystal. Because of the destructive nature of the bombardment event, open boundary conditions are used. In the limit of a semi-infinite crystal, atoms that pass through the sides and bottom of the collision region do not return, but rather are absorbed and incorporated into the bulk. Similarly, explicit energy-damping mechanisms are omitted, thus excess energy is removed by the expulsion of energetic particles. Finally, since it is beyond the scope of this paper to consider the ejection of bound dimers and larger multimers, only singly ejected Si atoms are included in the analysis.

ANALYSIS OF MOLECULAR-DYNAMICS DATA

The primary focus of this work is to elucidate the common mechanisms that give rise to features in the angular distributions of the ejected particles. In particular, we are interested in the relationship between angular distributions and the structural arrangement of the atoms in the near surface region, since our ultimate goal is to be able to use this technique to determine the structure of adsorbed overlayers on semiconductor surfaces. Experimentally it is possible to resolve the mass, energy, and ejection angles of the desorbed particles and in some systems the original layer of the atoms. For example, experiments have been performed on As-terminated

GaAs{001} surfaces where it is known that the first, third, etc. layers are As atoms and the second, fourth, etc. layers are Ga atoms, and it is experimentally possible to selectively detect Ga vs As species.[21,25,35,36] In addition, often the ejected ions are detected and these presumably more readily escape without being neutralized if they originate in layers closer to the surface. This feature enhances the selectivity of the experiment towards a specific layer in the substrate. Thus, in anticipation of the desire to examine properties by layer of origin, the yields of atoms ejected are presented accordingly in Table I. We have arbitrarily defined the layers by the vertical position. The values in Table I show that there are significant contributions to the ejected atom yield from as deep as layer four. This is not surprising since the open nature of the diamond lattice exposes more of the deeper layers of the crystal. In fact, an alternative definition of the first layer could be all atoms that are visible in Fig. 1, corresponding to a depth of 5 Å. With this alternative definition, virtually all the particles eject from the exposed layers as is the case for the close-packed metal surfaces.[15,20,37]

The global trends in the yields are fairly straightforward to understand. The 1× reconstructions have higher total yields than the 2× reconstructions. Possible explanations are (i) the dimerization process widens the channels for the primary particle to penetrate and not eject any atoms and (ii) the binding energy of the atoms in the dimerized surface is greater, thus fewer atoms can eject. The 4× reconstructions have more second-layer ejection because for part of the surface they are the topmost atoms.

The angle-integrated final kinetic-energy distribution for each surface reconstruction appears in Fig. 2. The shapes of these curves are similar with only small differences in peak positions and widths. In the past, much work has been devoted to relating features of energy-distribution curves to characteristic energetic parameters such as the bulk cohesive energy and surface binding energy.[12,15,20,38–41] These relationships are complicated, depending on bonding arrangements and collision dynamics and we feel that to attempt to interpret the energy distributions at such a level is beyond the scope of this paper. We find, however, that some mechanisms do depend on the energy of the ejecting particle, thus the distributions are shown for completeness. For the analyses given below, three energy ranges have been chosen which contain roughly equal numbers of ejected atoms, namely, 5–10, 10–20, and 20–50 eV. The very-low-energy particles are omitted, as they are hardest to measure and hardest to calculate reliably since they depend more sensitively on the correctness of the attractive portion of the interaction potential. The very-high-energy particles are omitted as the number of particles is low.

TABLE I. Yield of atoms ejected per 100 trajectories vs layer of origin of the atoms. For each surface a total of 2700 trajectories was calculated.

Surface	Total	Layer 1	Layer 2	Layer 3	Layer 4
(1×1)	94.6	54	19	19	1.5
(1×4)	83.2	36	25	16	6.0
(2×1)	61.1	26	21	10	3.7
(2×4)	61.9	19	26	11	5.5

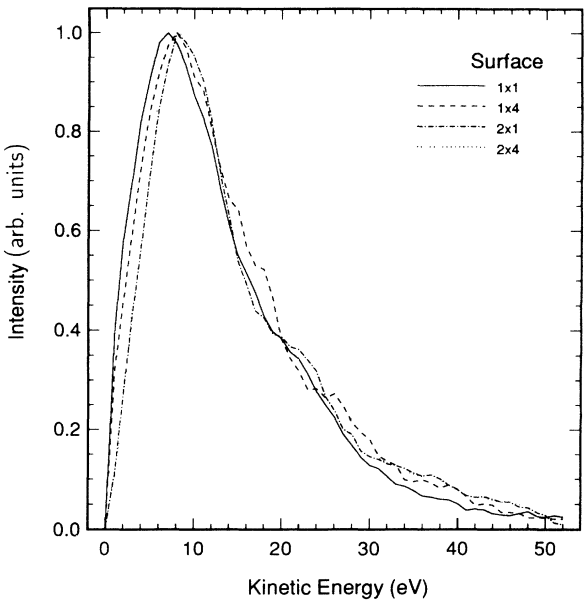

FIG. 2. Angle-integrated kinetic-energy distribution of ejected crystal atoms. The width of the energy bins used in the histogramming process is 2 eV. The maximum intensity in each plot has been normalized to unity.

The direction of the final velocity vector of an ejected atom is used to calculate its final polar angle Θ, and azimuthal angle Φ. The ejected atoms are separated into angular bins by scanning them with a "virtual" detector to produce distributions that are analogous to experimental results. Mathematically, the atoms that pass through a disk with diameter A_d located a distance L_d from the crystal are determined. This disk is oriented perpendicular to the direction vector defined by the detector polar and azimuthal angles as they are scanned through the region of interest. The values of A_d and L_d used in this work are 8 cm and 35 cm, respectively, which produces a polar acceptance angle of ca. $\pm 6.5°$. (The azimuthal acceptance angle, of course, varies as a function of polar angle.)

The polar-azimuthal-angular distributions of the ejected atoms for each surface reconstruction appear in Fig. 3. In this representation the intensities have been multiplied by $\sin(\Theta)$ so as not to overrepresent visually the small number of particles that eject normal to the surface. Since only trajectories in the unique portion of the surface unit cell are calculated, the surface symmetry is explicitly enforced on the angular distributions. These distributions include all atoms ejected in the range 5–50 eV and demonstrate the high degree of anisotropy observed for these systems. The (1×1) and (1×4) distributions have strong intensity features along the 0°,180° ($\langle 110 \rangle$) and 90°,270° ($\langle 1\bar{1}0 \rangle$) azimuths and are featureless elsewhere. The distributions for the dimerized (2×1) and

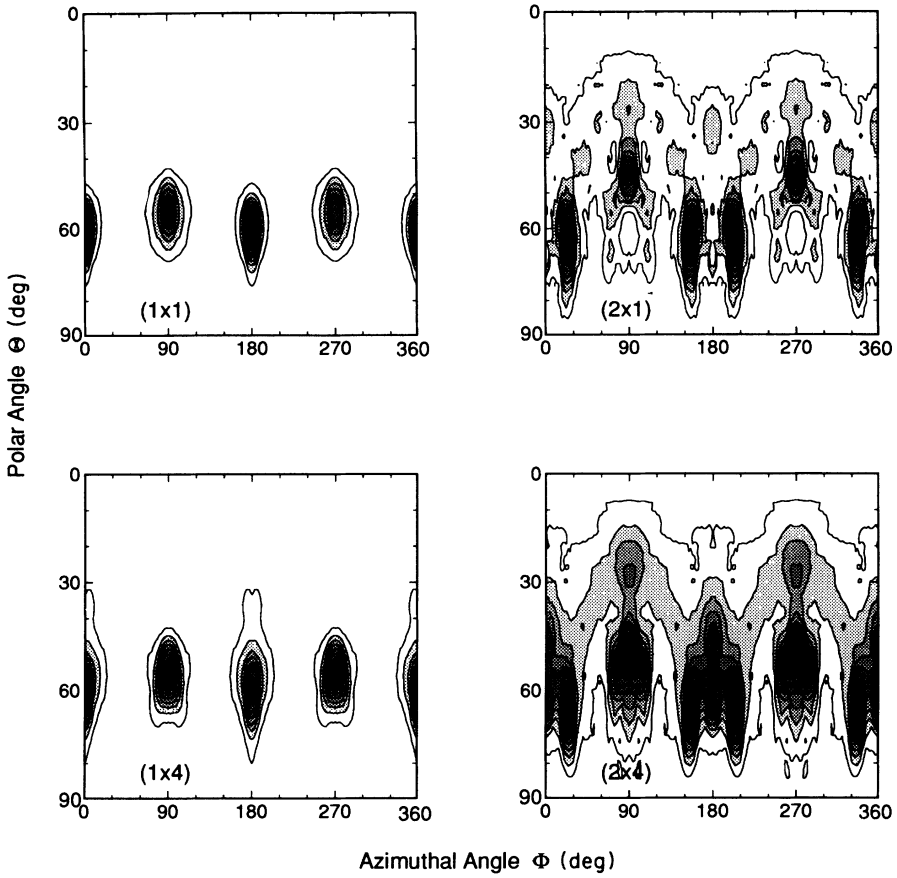

FIG. 3. Final polar-azimuthal-angle distributions of ejected crystal atoms. These distributions include all atoms ejected with energies in the range 5–50 eV. The maximum intensity in each plot has been normalized to unity. The contour values begin at 0.1 and are spaced 0.1 units apart, with areas of darker shading corresponding to higher intensity. The intensities are collected as described in the text and then multiplied by $\sin(\Theta)$ to convert to probability density.

(2×4) surfaces are similar, except for the strong intensity ca. 23° to either side of the 180° azimuth. These features apparently provide a signature for the dimer reconstructions; however, to confirm this we must further resolve the simulation results.

The results presented so far have been averaged over and it is hard to extract the features that might be sensitive to the surface structure. To fully resolve the simulation data, the ejected atom distributions must be segregated by two angles, energy, and layer of origin. This four-dimensional hypersurface would be difficult to visualize and analyze, thus judicious cuts along specific directions have been made to produce understandable, lower-dimensional representations. Using Fig. 3 as a guide, most of the interesting information appears to occur at or near certain key azimuthal angles. This idea is explored more fully in Figs. 4 and 5 where the polar-azimuthal-angular distributions for the (1×1) and (2×4) surfaces are resolved by the layer of origin. Alternatively, in Fig. 6 the polar distributions for the (1×1) surface separated by energy, azimuthal angle, and layer of origin are given. Before giving a more detailed discussion there are some obvious inferences to be drawn from Figs. 4 and 5. First, for the (1×1) surface (Fig. 4) the regions of high intensity (often referred to as peaks or spots) shift by 90° between layers. The third-layer ($L3$) contribution in Fig. 4 corresponds almost perfectly to the bond direction between third- and fourth-layer atoms. Analogously, the peak in the second-layer ($L2$) contribution is oriented along the bond direction between the second- and third-layer atoms, and the major peak in the first-layer ($L1$) contribution at $\Phi=180°$ is oriented along the bond direction between first- and second-layer atoms. The relation of the peaks in the $L1$ distribution at the 90° azimuth to the surface structure is not as obvious. The angular distribution from the (2×4) surface (Fig. 5) is remarkably similar with the notable exception that the peak at 180° in the $L1$ distribution has bifurcated.

We begin the detailed analysis with the unreconstructed (1×1) surface and examine its relatively simple angular distribution (Fig. 4). As reported previously[15,20,21,24] the two main features of the (1×1) distribution are two sharp intensity peaks at the 180° and 90° azimuths. Energy-resolved polar scans for atoms ejected from the first layer appear in Figs. 6(a) and 6(b). Recalling that the bond between a first- and second-layer atom lies along this azimuth, the intensity profile [Fig. 6(a)] suggests that the origin of the peak may arise from a direct neighbor-neighbor collision. The peak position in the polar-angle distribution depends on energy. The peak for the highest-energy atoms approaches the ideal bond angle of ca. 55°, while the peak at lower energies occurs at more grazing angles. This behavior may indicate that the ejecting atoms are interacting with adjacent surface atoms after the initial momentum transfer or, alternatively, that the direction of the momentum transfer varies as a function of collision energy. The first-layer distribution also has an intense feature along the 90° azimuth [Fig. 6(b)] at a polar angle of ca. 52°. The peak position in this case shows no measurable dependence on the energy, nor

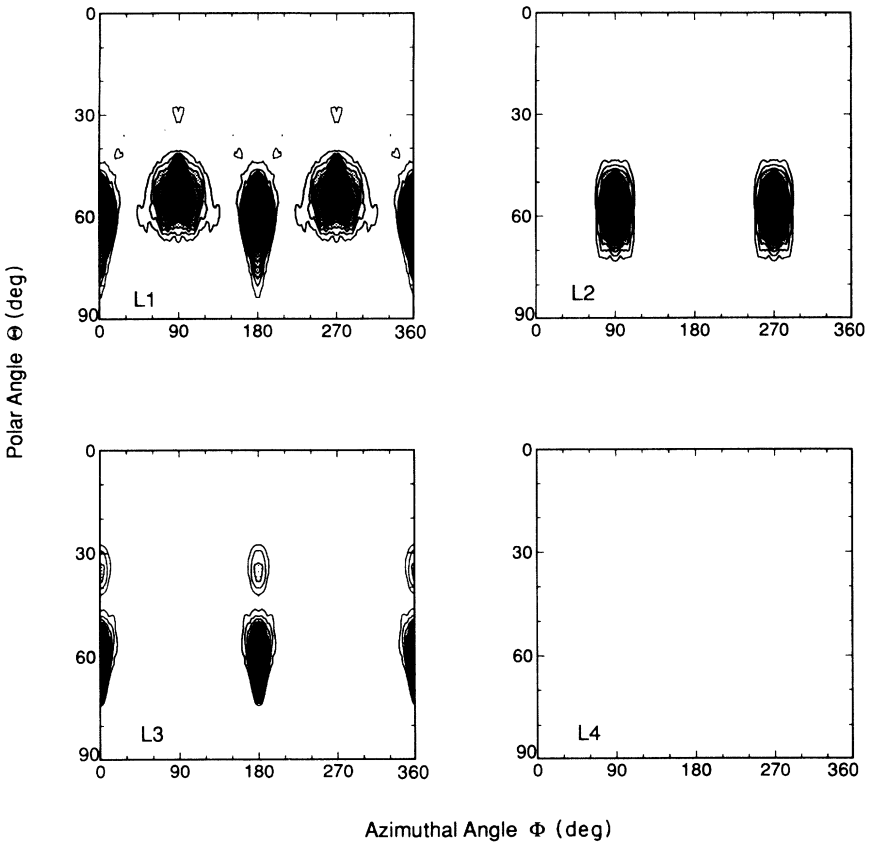

FIG. 4. Layer-resolved, final polar-azimuthal-angle distributions of atoms ejected from the (1×1) surface. These distributions include all atoms ejected with energies in the range 5–50 eV. The distributions for all layers were subject to the same normalization and are directly comparable. The contour values begin at 4 and are spaced two units apart, with areas of darker shading corresponding to higher intensity. The intensities are collected as described in the text and then multiplied by sin(Θ) to convert to probability density.

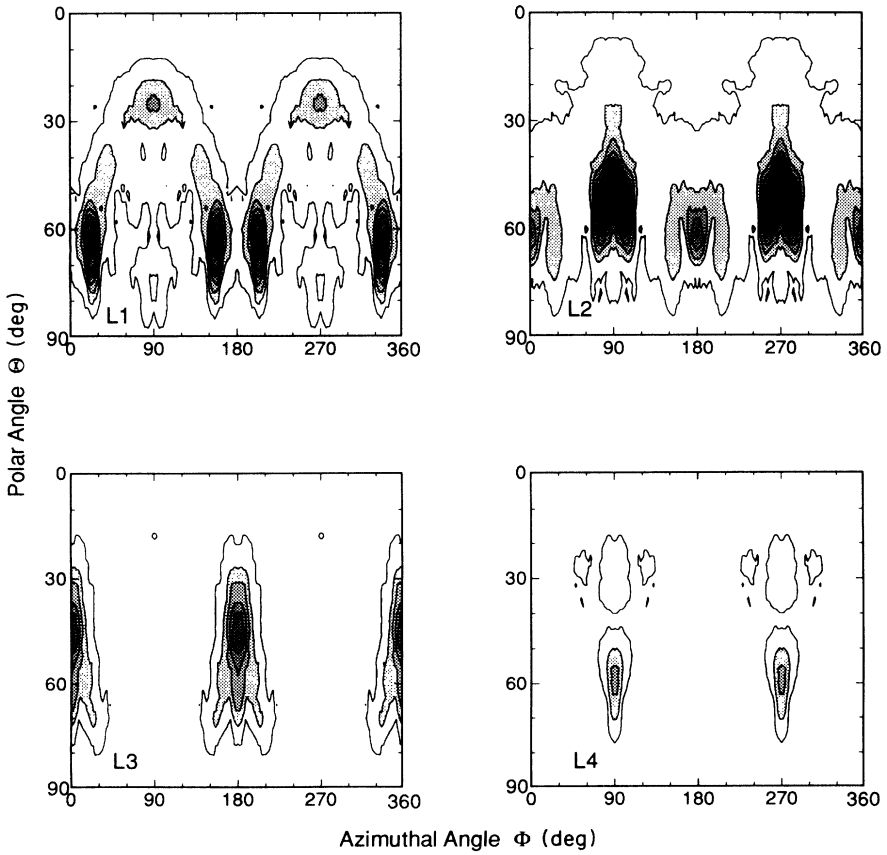

FIG. 5. Layer-resolved, final polar-azimuthal-angle distributions of atoms ejected from the (2×4) surface. These distributions include all atoms ejected with energies in the range 5–50 eV. The distributions for all layers were subject to the same normalization and are directly comparable. The contour values begin at 4 and are spaced two units apart, with areas of darker shading corresponding to higher intensity. The intensities are collected as described in the text and then multiplied by sin(Θ) to convert to probability density.

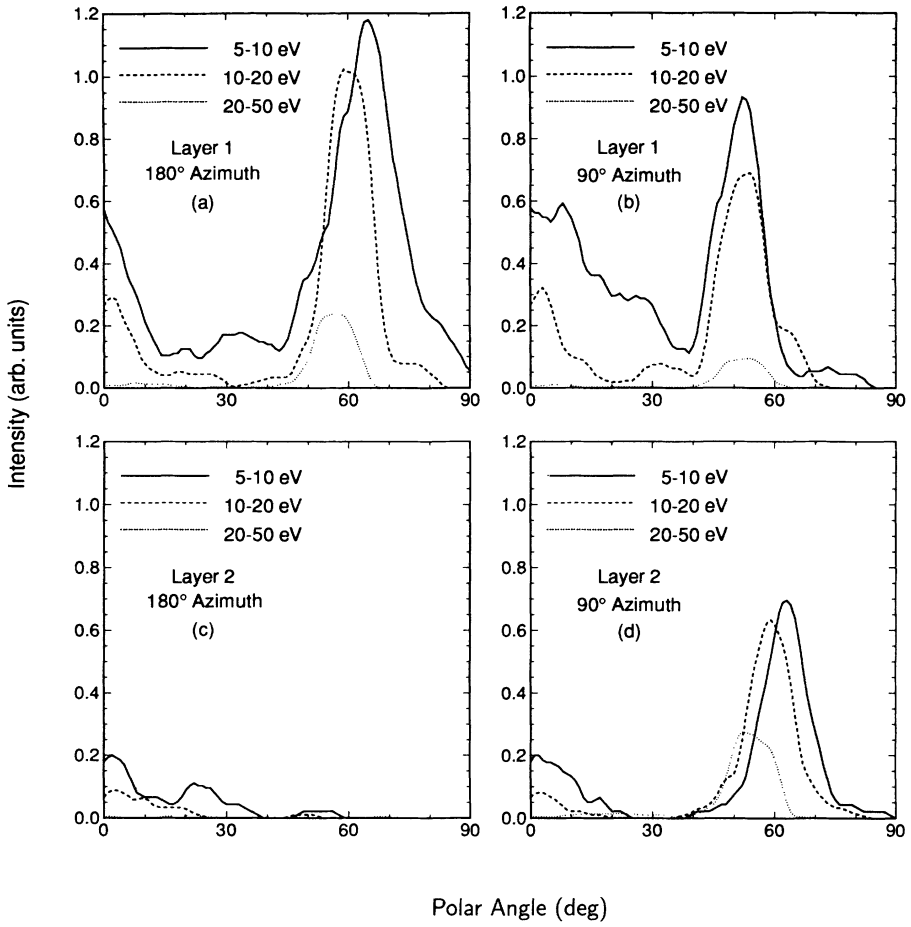

FIG. 6. Layer- and energy-resolved polar-angle distributions for atoms ejected from the (1×1) surface. The three curves in each plot correspond to atoms ejected within the three energy ranges denoted in the figure. Each curve is divided by the width of its energy range to approximate scale to the average number of atoms per energy bin. Although these units are arbitrary, the scaling among all four frames is not. These curves do not have the $\sin(\Theta)$ conversion factor, thus the intensity at $\Theta=0°$ appears high.

does its direction correspond to any nearest-neighbor geometry. To fully understand the origin of these two peaks the ejection process needs to be examined at the atomic level.

The observation that there are highly oriented ejection directions of the atoms implies that there is some common atomic motion, even though there are a multitude of different atoms that contribute to each high-intensity region in the angular distributions. The challenge is to extract the common dominant mechanisms. After examining the full dynamics of many collision cascades, we determined that the last two collisions before an atom ejects are the important ones. These collisions are the one that knocks out the atom and the one that initiates this motion. The multitudes of motions that occur at the beginning of the collision cascade are considerably less important for the specific ejection event.

The essential information for the graphs of the motion is determined by a method developed by Harrison,[42] which he termed "lean-on," a colloquial expression for a collision. If only pair potentials are used for the interactions among the atoms, it is relatively straightforward to define a collision as occurring when two atoms have potential energy greater than a specified value, typically slightly greater than zero for these highly energetic collisional processes. Past experience using this definition shows that it highlights the key factors for atomic motion except for changes in direction driven by attractive interactions, e.g., the pull of an atom towards the surface as it ejects. Ambiguity results when attempting to adapt this definition to many-body potentials as the energy is no longer simply a function of the positions of two atoms, but rather depends also on the positions of other nearby atoms. To obtain the information we require, we have arbitrarily decided to use a repulsive Molière potential to define a collision. Thus, at each integration step we check to see if the Molière interaction between a pair of atoms is greater than a threshold value. If this is true, then we define a collision within the lean-on tree. If, in fact, the mechanistic interpretation of the important collisional events appears to be too sensitive to this arbitrary definition, then the atomic motions must be examined more carefully.

For each trajectory in the simulation a lean-on tree is determined. Initially the primary particle (Ar^+ ion) strikes one of the substrate atoms, then each of these two species can undergo further collisions. At each integration step the positions and velocities are saved for only the atoms that are part of the lean-on tree. For example, at the first integration step the initial positions are saved. Once the Ar^+ ion strikes another substrate atom, the positions and velocities of these two atoms are saved at all subsequent steps. Of note is that once an atom becomes part of the tree it does not get removed even though it may no longer be colliding with another atom. Disk storage is greatly reduced by saving only the step infor-

mation of atoms that undergo collisions. Since we create this information for each Ar^+-ion impact, the files are periodically transferred to tape. This lean-on analysis has no influence on the integration process.

After calculation and analysis of all trajectories, a set of atoms that has ejected is chosen for use in mechanistic elucidation. Since the atom number and trajectory number are known, we have written a program that scans through the saved lean-on information and extracts the positions and velocities of the three atoms (trace atoms) involved in the last two collisions.

To illustrate this approach, we first examine the dominant sequence of collisions, which leads to the ejection of a particular atom from a (1×1) surface. The intensity along the 180° azimuth (Fig. 4) arises from the ejection of first- and third-layer atoms. It is simplest to start with first-layer atoms. One trajectory for $L1$ atoms from each energy range of Fig. 6(a) is shown in Figs. 7(a)–7(c). Each plot has two parts, the first being many atoms in the near region in their initial positions (prior to bombardment) and the second being the positions of the three trace atoms shown at 5-fs (1 fs$=10^{-15}$ s) intervals. The radius of the trace atoms is proportional to their instantaneous total (kinetic+potential) energy. The fixed crystal atoms are drawn with a radius which is equivalent to 40 eV of total energy. Essential information of the positions and energy of the trace atoms during the collision sequence is depicted in a compact form. Moreover, the irrelevant motions of the remainder of the atoms are not shown and thus do not visually detract from the motions of interest. This graphical representation is sufficiently simple that virtually all the ejection events can be viewed in order to obtain a total perspective of the important collisions.

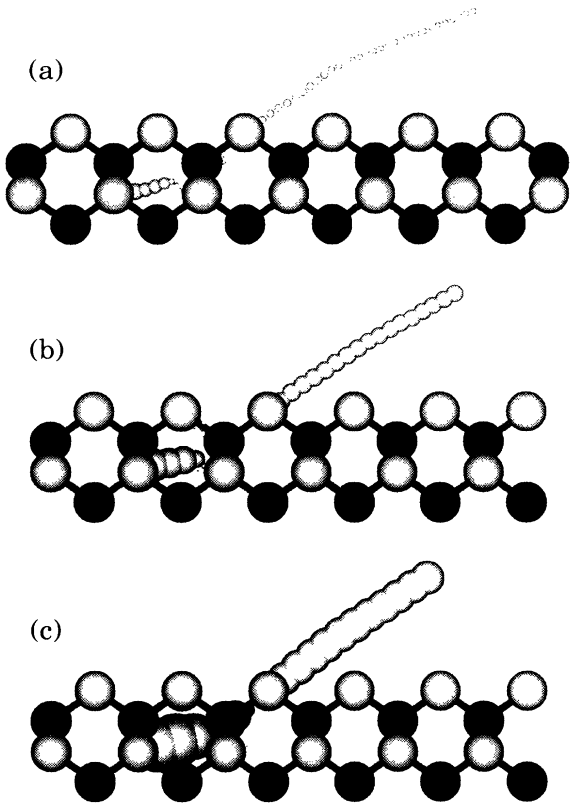

FIG. 7. Time-lapse representation of trajectories leading to ejection of first-layer atoms from the (1×1) surface along the 180° azimuth. Only the motion of the last three atoms in the collision sequence is shown. Sizes of the moving atoms reflect their instantaneous total (kinetic+potential) energy and their positions are plotted at 5-fs intervals. The size of the rigid crystal atoms is equivalent to a 40-eV total energy. The atom from the third layer (light sphere) hits the atom from the second layer (dark sphere), and the final momentum transfer from the second-layer atom to the first-layer atom along the bond axis is very fast. The view angle is parallel to the $\langle 110\rangle$ or 180° azimuth. The final kinetic energy of the ejected particle is about (a) 5, (b) 20, and (c) 35 eV.

The trajectories shown in Fig. 7 clearly demonstrate that the $L1$ contribution to the intensity along the 180° azimuth arises from a direct neighbor-neighbor collision between a first- and second-layer atom. The energy dependence of the polar peak position is attributable to interaction with neighboring surface atoms. For an atom that ejects with about 35 eV [Fig. 7(c)] the motion is undeflected, indicating minimal influence of the surface atoms. As the asymptotic energy decreases [Figs. 7(b) and 7(a)], the influence of the attractive interaction to the surface is increased and the atomic motion bends toward the surface. Of note is that the third-layer atom that initiates the motion is not bonded to the second-layer atom. In summary, it is direct collisions with bonded second-layer atoms that characterize the ejection process of first-layer atoms in the 180° direction. Since the last collision involves an atom from the adjacent layer we will refer to it as the Δ_1 mechanism.

Examples of the atomic motion which lead to ejection of first-layer atoms along the 90° azimuth are shown in Fig. 8. A systematic survey of the pertinent trajectories reveals that ejection in this direction is due to a fourth-layer substrate atom, which travels through an open channel of the crystal and strikes a first-layer atom. From Fig. 1 it is apparent that first- and fourth-layer atoms lie in the same planes along the 90° azimuth. The fourth-layer atom travels in the narrow channel formed by the third- and second-layer atoms (along the direction of the bond between atoms in the third and second layers) before hitting the first-layer atom. As was seen for the 180° azimuth the ejecting atom interacts with neighboring surface atoms, however, here the effect on the final angle does not seem to depend on energy [Figs. 6(c) and 6(d)]. For all three energy ranges the polar peak position is at ca. 52°. We do not wish to belabor the differences here, except to say that they reflect the directional nature of the potential-energy function. Motion of an ejecting first-layer atom towards another first-layer atom along the 90° azimuth tends to lower the energy (near dimer formation), and the trajectories, in fact, show an initial horizontal acceleration before the atom is deflected away from the surface. In contrast, motion along the 180° azimuth introduces bond angle strain and the atom initially accelerates away from the surface. After bonds to the second layer are broken the ejecting atom is pulled into a more grazing altitude by an adjacent first-layer atom.

However, by far the most interesting characteristic of the 90° mechanism is that it involves long-range motion of atoms through the substrate. Since it involves atoms separated by three layers it will be referred to as the Δ_3 mechanism.

That atoms can move relatively unrestricted through the diamond-lattice structure is hardly surprising given its low packing density (67% open space)[43] and it is, therefore, also not surprising that large numbers of atoms from layers 2–4 are ejected. Based on the knowledge of how first-layer atoms eject and the observation of the openness of the crystal, it is interesting to speculate on what might occur for ejection of atoms from deeper layers. A collision between a third-layer atom and a second-layer atom, resulting in the ejection of the second-layer atom along the bond direction (Δ_1 mechanism), should result in high intensity along the 90° azimuth as clearly seen in Fig. 4. It is crucial to realize that second-layer atoms energized by this direct mechanism have no obstacles in their exit channels. Similarly, third-layer atoms should have no obstacles when exiting along the third- to fourth-layer bond axis (the 180° azimuth as seen in Fig. 4). However, as shown in Fig. 8, fourth-layer atoms which are energized by the Δ_1 mechanism do encounter an impediment, a first-layer atom. Likewise, atoms from the second layer which are energized by the Δ_3 mechanism and attempt to eject along the 180° azimuth will be stopped by a neighboring first-layer atom. The polar-angle distributions for ejected second-layer atoms shown in Figs. 6(c) and 6(d) confirm the ideas discussed above. The intensity along the 90° azimuth shows the characteristic shift in peak position with energy of the direct mechanism. These speculations are, in fact, confirmed by a detailed survey of the trajectories.

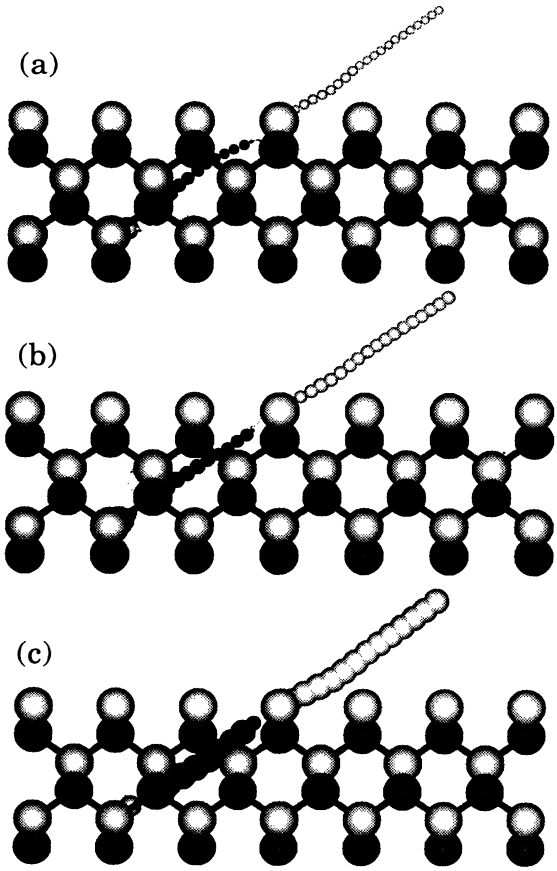

FIG. 8. Time-lapse representation of trajectories leading to ejection of first-layer atoms from the (1×1) surface along the 90° azimuth. See caption to Fig. 7. The atom from the fifth layer (light sphere) hits the atom from the fourth layer (dark sphere), and the final momentum transfer is from the fourth-layer atom to the first-layer atom. The view angle is parallel to the $\langle 1\bar{1}0 \rangle$ or 90° azimuth.

Based upon the observations for the (1×1) surface, we now propose that the ejection of atoms from the {001} face of a diamond lattice is controlled by only two basic mechanisms. The first is the collision between two nearest neighbors, which has been labeled Δ_1, and the second is the collision between atoms separated by three interlayer distances, which has been labeled Δ_3. Since only those trajectories that contribute to the major features have been surveyed, there may be other minor mechanisms. One example of this is atoms that eject at polar angles close to the surface normal. A variety of different mechanisms is observed here, however, the total number of atoms ejected at low polar angles is small. In the remainder of this paper the influence of surface morphology on the nature of the Δ_1 and Δ_3 mechanisms and the resulting angular distributions are discussed.

Polar-angle distributions of atoms ejected for the first two layers of the four surface reconstructions are shown in Fig. 9. Here all atoms with final energies in the range 5–50 eV are included since the fundamental ejection mechanisms are independent of energy. Starting first with the (1×4) reconstruction, the distributions for first-layer atoms [Figs. 9(a) and 9(b)] are observed to be similar to those shown for the (1×1) surface. Not surprisingly the Δ_1 and Δ_3 mechanisms are responsible for the 180° and 90° peaks, respectively. The differences in the peak heights between the first-layer scans from the (1×1) and (1×4) surfaces are a direct reflection of the relative number of surface atoms.

It is with the polar-angular distributions of atoms from the second layer, shown in Figs. 9(c) and 9(d), that the effect of the missing row in the (1×4) reconstruction becomes apparent. The most obvious feature here is the appearance of a signal at high polar angles along the 180° azimuth. By removing every fourth row of first-layer atoms, the channel for the Δ_3 mechanism for the ejection of second-layer atoms opens up. The trajectories shown in Fig. 10 confirm the Δ_3 mechanism for this peak and also offer insight into why these atoms exist at such high polar angles, rather than 55° as observed for the first-layer atoms. As the atoms move across the missing row, they are in close proximity to several first- and second-layer atoms and are pulled toward the surface. The effect varies with energy and not surprisingly the greatest deflection is seen for the lowest-energy atoms. More importantly, because of our knowledge of the ejection mechanism, it is possible to predict the effect a change in surface morphology will exert on the trajectory. Another mechanism, shown in Fig. 11, contributes to the 180° az-

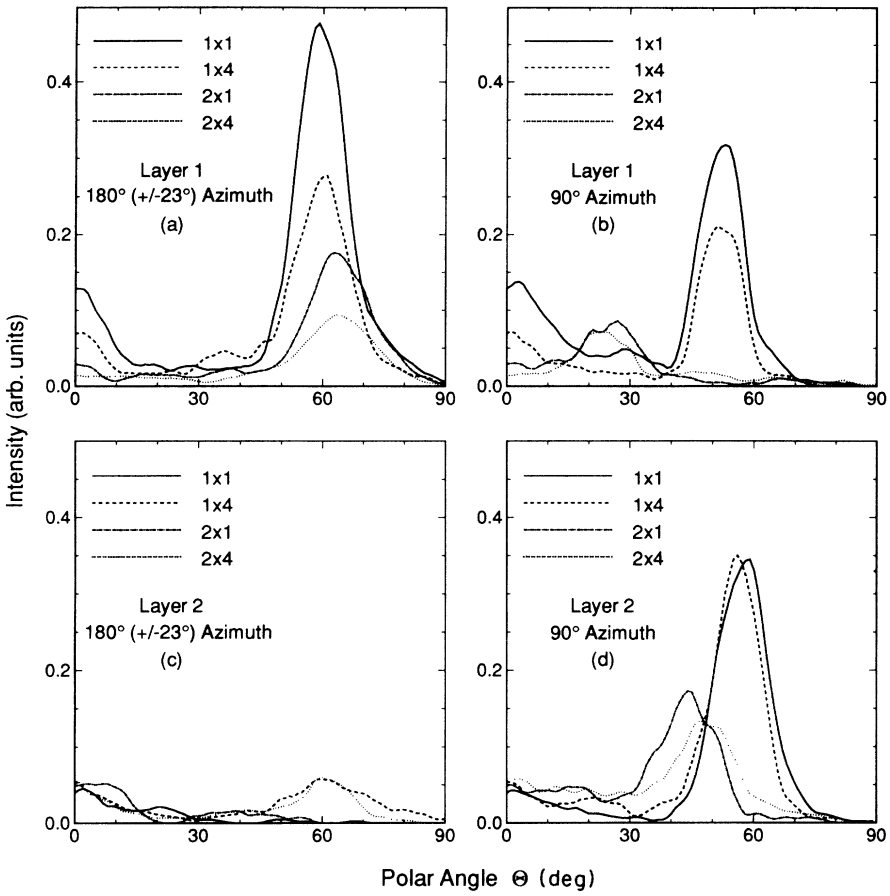

FIG. 9. Layer-resolved polar-angle distributions for atoms ejected from the crystal. The four curves shown in each plot correspond to the four surface reconstructions studied in this work. The normalization is the same as in Fig. 6. The energy range of the particles is 5–50 eV.

imuth intensity. In this case it is a third-layer atom, which travels diagonally and collides with a second-layer atom. This mechanism was actually shown before in Fig. 7 where it initiated the Δ_1 ejection of first-layer atoms from the (1×1) surface; however, on the (1×4) surface those second-layer atoms adjacent to the missing row are no longer blocked.

A strong third-layer intensity feature is also observed along the 180° azimuth for the (1×4) surface and is due to Δ_1 ejections. [This is not shown but is very similar to the (2×4) $L3$ and $L4$ data in Fig. 5.] Because of the missing row of first-layer atoms on the (1×4) surface it is also possible for significant numbers of fourth-layer atoms to escape the surface. The angular distributions for these atoms peak along the 90° azimuth and the atoms are again ejected via the Δ_1 mechanism. It is thus the appearance of a fourth-layer signal and the 180° azimuth second-layer signal that distinguishes the (1×4) and (1×1) results. Unfortunately, both of these features are relatively weak (compared to the major intensity features) and may be difficult to observe experimentally. Introduction of the dimer reconstruction in the (2×1) and (2×4) surfaces, however, produces more obvious changes that can be observed in the ejection patterns.

The angular distributions for the (2×1) and (2×4) surfaces are similar to each other (Fig. 3). The only important differences are the appearance in the (2×4) distribution of a second-layer signal in the 180° azimuth and a fourth-layer signal in the 90° azimuth. These new features are analogous to what is discussed above in going from the (1×1) to the (1×4) distribution. For this reason the remainder of the discussion will emphasize the (2×4) data and the differences between the dimerized and undimerized reconstructions.

The (2×4) contours for first-layer atoms, shown in Fig. 5, indicate that the 180° azimuth intensity feature seen on the (1×1) distribution (Fig. 4) is now split into two features ca. 23° to either side of the 180° azimuth. Correspondingly, the polar-angle scans shown in Fig. 9(a) are taken along the 180°±23° azimuth instead of the 180° azimuth. The reason for this splitting is directly related to the dimer reconstruction. In this reconstruction two atoms that would be second-nearest neighbors in the bulk (separated by 3.84 Å) bond together with a separation distance of 2.4 Å. This surface reconstruction results in a bond between the first- and second-layer atoms, which is oriented at a polar angle of ca. 65° and an azimuthal alignment of 180°±23°. The Δ_1 mechanism, as shown in Fig. 12 with this geometry, results in the high-intensity regions shown in Figs. 5 and 9(a). The polar scans shown in Fig. 9(b) for the 90° azimuth have a strong signal at a polar angle of ca. 25°. As a result of the dimerization the strong feature at 52° is shifted to 25°. This intensity is produced by two versions of a Δ_3 mechanism,

as shown in Fig. 13. The mechanism in Fig. 13(a) is analogous to the Δ_3 observed for the (1×1) surface shown in Fig. 8. The mechanism in Fig. 13(b) is similar, but relies on the dimer reconstruction to place the first-layer atom in the path of the impinging fourth-layer atom. Like the missing row, the dimer reconstruction makes characteristic modifications to basic Δ_1 and Δ_3 mechanisms.

There are notable differences between distributions of second-layer atoms from the (1×1) and (2×4) surfaces. The (1×1) intensity (Fig. 4) forms a single, well-defined spot, which is centered along the 90° azimuth at a polar angle of ca. 60°. Intensity along this direction for the (2×4) surface occurs at a smaller polar angle of ca. 45°. In addition, the dimerized surface exhibits shoulder peaks about the 90° azimuth, which extend to higher polar angles. These features are easily understood by considering the environments of second-layer atoms in the dimerized and undimerized reconstructions. In the (1×1) surface all second-layer atoms are equivalent and atoms that eject along either the 90° or 270° azimuth will travel equivalent paths. Likewise, all second-layer atoms are equivalent on the (2×1) surface; however, there are two different ejection pathways. For a particular atom, one direction involves passing between a pair of surface dimers and the other involves passing over the empty trough created by the dimerization. Removal of every fourth row to form the (1×4) and (2×4) surfaces reduces the symmetry even further, resulting in four inequivalent pathways for second-layer atoms ejecting from the (2×4) surface.

These inequivalent pathways manifest themselves in the angular distributions as two classes of Δ_1-type ejection mechanisms. The first corresponds to those atoms which pass between the surface dimer pairs and which are denoted as Δ_{1D}. The sharp feature of the (2×4) distribution along the 90° azimuth at a polar angle of ca. 50° is due almost exclusively to these atoms. In fact, passing between the dimers focuses the atoms so that they exit within a very narrow range of polar and azimuthal an-

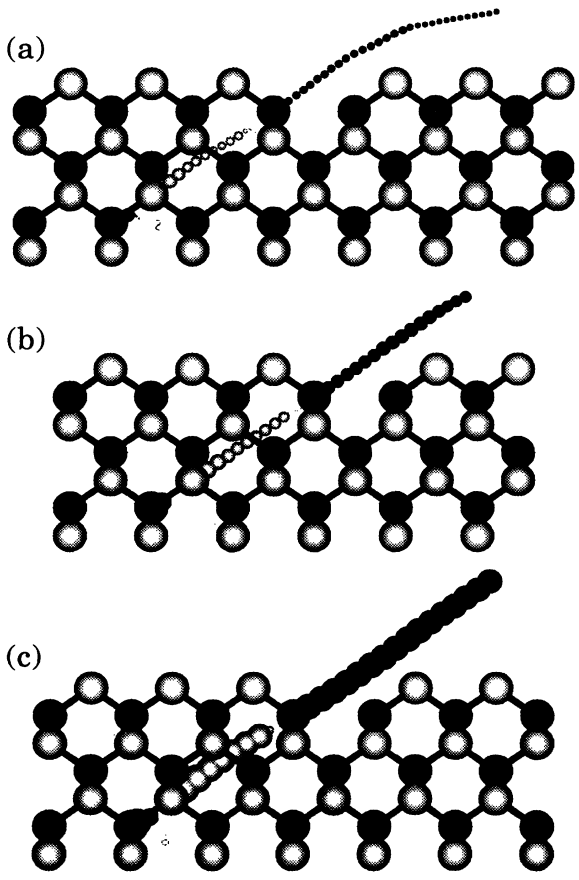

FIG. 10. Time-lapse representation of trajectories leading to ejection of second-layer atoms from the (1×4) surface along the 180° azimuth. See caption to Fig. 7. The atom from the sixth layer (dark sphere) hits the atom from the fifth layer (light sphere), and the final momentum transfer is from the fifth-layer atom to the second-layer atom. The view angle is parallel to the $\langle 1\bar{1}0 \rangle$ or 90° azimuth. The missing row is apparent in each frame slightly right of center.

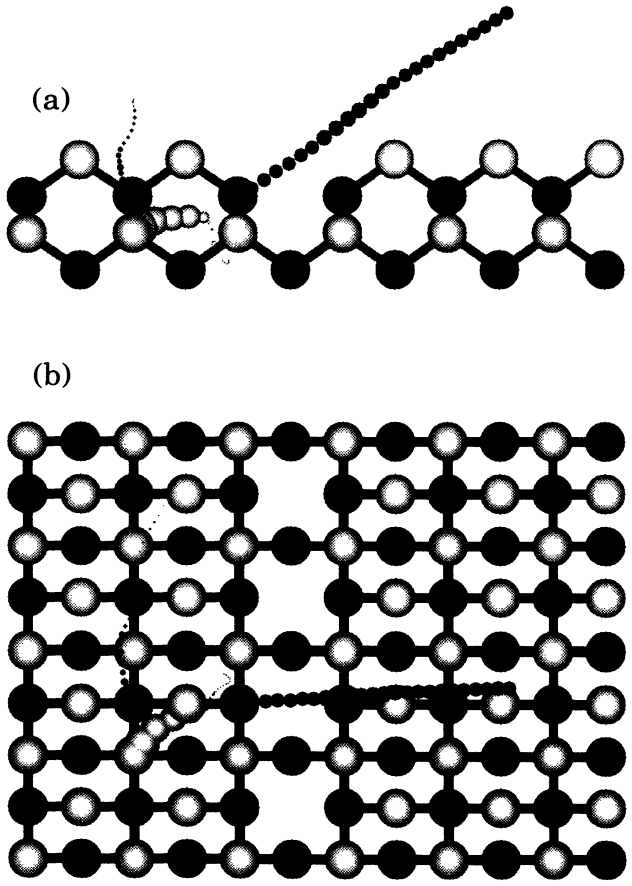

FIG. 11. Time-lapse representation of trajectory leading to ejection of a second-layer atom from the (1×4) surface along the 180° azimuth. See caption to Fig. 7. The atom from the third layer (light sphere) gets deflected by the second-layer atom (dark sphere), and the final momentum transfer is from the deflected third-layer atom to the second-layer atom. A side (upper) and top (lower) view of the same trajectory is presented. The energy of the particle is about 10 eV.

gles. The second class consists of atoms which exit over the troughs (i.e., all atoms which do not pass between the dimers); these are denoted as Δ_{1T}. There is not a strong focusing process and the angular distribution is more diffuse. The characteristic shoulders result from attractive interactions as the ejecting atoms pass across an adjacent row of surface dimers.

CONCLUSIONS

We have developed a compact and efficient graphical method for analyzing the key atomic motions in molecular-dynamics simulations. There are two features that distinguish our approach from others. First, the atoms that are directly involved in the collisions are determined during the course of the numerical integration. Only the positions and velocities of these atoms are saved at intermediate time steps. This greatly reduces the disk storage required and, consequently, we can readily store the output from several hundred trajectories. Second, the picture of the motion isolates the time sequence of the positions and energy of only three important atoms. The remainder of the atoms are shown at their initial positions. With this compact representation it is easy to examine two different trajectories and determine whether they are the same or different. A large number of trajectories can be surveyed in a brief time period.

We have applied this method for mechanistic analysis to a systematic investigation of the effect of missing rows and dimerization in the various surface reconstructions of the Si{001} surface on the angular distributions of the ejected atoms. The work presented here illustrates that there are two basic ejection mechanisms, which can characterize the complicated dynamics of keV-particle bombardment of semiconductors. A Δ_1 mechanism has been identified in which an atom in the substrate moves along the bond direction with an atom in the next-higher layer forcing it to eject. A Δ_3 mechanism has been identified in which an atom three layers below moves through an open channel before knocking out an atom. These two mechanisms are by no means all the motions in the solids, but rather are the dominant ones that give rise to ejection.

One goal is to be able to determine structures of adsorbates on semiconductor surfaces by measuring the angular distributions of the particles that eject. Based on the analysis given here of the underlying ejection mechanisms we believe this goal is feasible. For example, if an adsor-

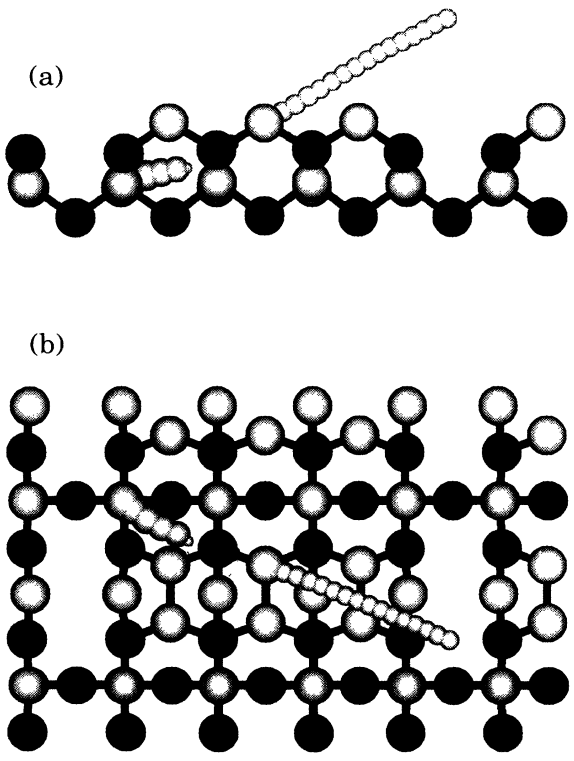

FIG. 12. Time-lapse representation of trajectory leading to ejection of a first-layer atom from the (2×4) reconstruction along the 180°+23° azimuth. See caption to Fig. 7. The atom from the third layer (light sphere) hits the atom from the second layer (dark sphere), and the final momentum transfer from the second-layer atom to the first-layer atom is very fast along the bond axis. A side (upper) and top (lower) view of the same trajectory is presented.

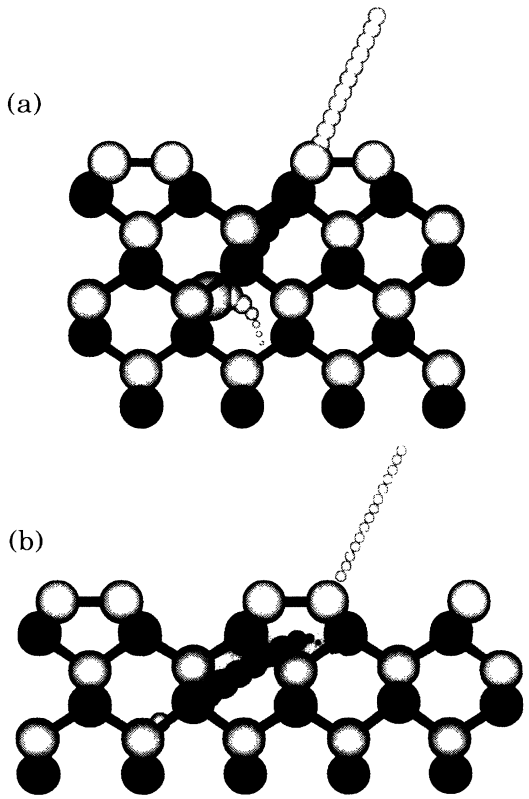

FIG. 13. Time-lapse representation of trajectories leading to ejection of first-layer atoms from the (2×4) reconstruction along the 90° azimuth. See caption to Fig. 7. The atom from the fifth layer (light sphere) hits the atom from the fourth layer (dark sphere), and the final momentum transfer is from the fourth-layer atom to the first-layer atom.

bate bonds in the fourfold hollows along the dimer row in the (2×4) reconstruction, the intensity of Ga atoms ejecting through the dimers will be diminished. If the adsorbate atom goes into the missing row then the intensity of ejecting Ga atoms in the 180° azimuth will be reduced. The possibility of predicting the height of the adsorbate atoms above the surface may also be possible for some of the binding sites.

ACKNOWLEDGMENTS

The financial support of the Office of Naval Research and the National Science Foundation is gratefully acknowledged. The Pennsylvania State University supplied a generous grant of computer time for these studies. We would also like to thank Steve Goss, Xu Chen, and Nicholas Winograd for insightful discussions.

*Present address: Horizon Systems, Inc., Stamford, CT 06903.

[1]See, for example, N. Winograd and B. J. Garrison, in *Ion Spectroscopies for Surface Analysis,* edited by A. W. Czanderna and D. Hercules (Plenum, New York, 1991), pp. 45–141, and references therein.

[2]R. Webb, R. Smith, E. Dawnkaski, B. Garrison, and N. Winograd, International Video Journal of Engineering Research (Gordon and Breach, New York, 1994).

[3]B. J. Garrison, N. Winograd, and D. E. Harrison, Jr. (unpublished).

[4]R. P. Webb and D. E. Harrison, Jr., Nucl. Instrum. Methods B **218**, 727 (1983).

[5]M. Shapiro and T. A. Tombrello (unpublished).

[6]H. Feil (unpublished).

[7]D. E. Harrison, Jr. and C. B. Delaplain, J. Appl. Phys. **47**, 2252 (1976).

[8]N. Winograd, B. J. Garrison, and D. E. Harrison, Jr., J. Chem. Phys. **73**, 3473 (1980).

[9]B. J. Garrison, J. Am. Chem. Soc. **102**, 6553 (1980).

[10]B. J. Garrison, N. Winograd, and D. E. Harrison, Jr., J. Chem. Phys. **69**, 1440 (1978).

[11]S. P. Holland, B. J. Garrison, and N. Winograd, Phys. Rev. Lett. **43**, 220 (1979).

[12]C.-C. Chang, Phys. Rev. B **48**, 12 399 (1993).

[13]M. H. Shapiro and T. A. Tombrello, Nucl. Instrum. Methods B **84**, 453 (1994).

[14]B. J. Garrison, N. Winograd, D. M. Deaven, C. T. Reimann, D. Y. Lo, T. A. Tombrello, D. E. Harrison, Jr., and M. H. Shapiro, Phys. Rev. B **37**, 7197 (1988).

[15]R. Smith, D. E. Harrison, Jr., and B. J. Garrison, Phys. Rev. B **40**, 93 (1989).

[16]R. Maboudian, Z. Postawa, M. El-Maazawi, B. J. Garrison, and N. Winograd, Phys. Rev. B **42**, 7311 (1990).

[17]S. P. Holland, B. J. Garrison, and N. Winograd, Phys. Rev. Lett. **43**, 220 (1979).

[18]C. T. Reimann, K. Walzl, M. El-Maazawi, D. M. Deaven, B. J. Garrison, and N. Winograd, J. Chem. Phys. **89**, 2539 (1988).

[19]C. T. Reimann, M. El-Maazawi, K. Walzl, B. J. Garrison, N. Winograd, and D. M. Deaven, J. Chem. Phys. **90**, 2027 (1989).

[20]R. A. Stansfield, K. Broomfield, and D. C. Clary, Phys. Rev. B **39**, 7680 (1989).

[21]R. Blumenthal, K. P. Caffey, E. Furman, B. J. Garrison, and N. Winograd, Phys. Rev. B **44**, 12 830 (1991).

[22]B. J. Garrison, C. T. Reimann, N. Winograd, and D. E. Harrison, Jr., Phys. Rev. B **36**, 3517 (1987).

[23]R. S. Taylor and B. J. Garrison, J. Am. Chem. Soc. **116**, 4465 (1994).

[24]R. J. MacDonald, Phys. Lett. **29A**, 256 (1969); Radiat. Eff. **3**, 131 (1970); Philos. Mag. **21**, 519 (1970).

[25]K. Caffey, R. Blumenthal, J. Burnham, E. Furman, and N. Winograd, J. Vac. Sci. Technol. B **9**, 2268 (1991).

[26]J. S. Burnham, D. E. Sanders, C. Xu, R. M. Braun, S. H. Goss, K. P. Caffey, B. J. Garrison, and N. Winograd (unpublished).

[27]H. E. Farnsworth, R. E. Schlier, T. H. George, and R. M. Burger, J. Appl. Phys. **29**, 1150 (1958).

[28]J. H. Neave and B. A. Joyce, J. Cryst. Growth **44**, 387 (1978).

[29]P. Drathen, W. Ranke, and K. Jacobi, Surf. Sci. **77**, L162 (1978).

[30]M. D. Pashley, K. W. Haberen, W. Friday, J. M. Woodall, and P. D. Kirchner, Phys. Rev. Lett. **60**, 2176 (1988).

[31]D. K. Biegelsen, R. D. Bringans, J. E. Northrup, and L. E. Swartz, Phys. Rev. B **41**, 5701 (1990).

[32]D. E. Harrison, Jr., in *Critical Reviews in Solid State and Materials Sciences,* edited by J. E. Green (CRC, Boca Raton, 1988), Vol. 14, Suppl. 1.

[33]B. J. Garrison, Chem. Soc. Rev. **21**, 155 (1992).

[34]J. Tersoff, Phys. Rev. B **37**, 6991 (1988); **39**, 5566 (1989).

[35]R. Blumenthal and N. Winograd, Phys. Rev. B **42**, 11 027 (1990).

[36]C. Xu, K. P. Caffey, J. S. Burnham, S. H. Goss, B. J. Garrison, and N. Winograd, Phys. Rev. B **45**, 6776 (1992).

[37]D. E. Harrison, Jr., P. W. Kelly, B. J. Garrison, and N. Winograd, Surf. Sci. **76**, 311 (1978).

[38]P. Sigmund, Phys. Rev. **184**, 383 (1969).

[39]M. W. Thompson, Philos. Mag. **18**, 377 (1968).

[40]B. J. Garrison, N. Winograd, D. Lo, T. A. Tombrello, M. H. Shapiro, and D. E. Harrison, Jr., Surf. Sci. Lett. **180**, L129 (1987).

[41]B. J. Garrison, Nucl. Instrum. Methods B **17**, 305 (1986).

[42]This terminology dates back at least to 1977 when we inherited the computer code.

[43]N. W. Ashcroft and N. D. Mermin, *Solid State Physics* (Holt, Rinehart and Winston, New York, 1976), p. 83.

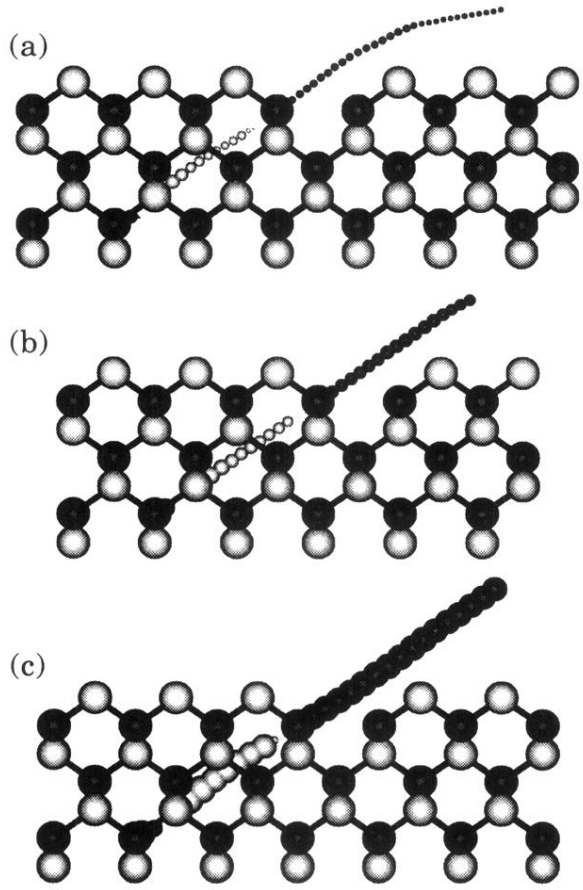

FIG. 10. Time-lapse representation of trajectories leading to ejection of second-layer atoms from the (1×4) surface along the 180° azimuth. See caption to Fig. 7. The atom from the sixth layer (dark sphere) hits the atom from the fifth layer (light sphere), and the final momentum transfer is from the fifth-layer atom to the second-layer atom. The view angle is parallel to the $\langle 1\bar{1}0\rangle$ or 90° azimuth. The missing row is apparent in each frame slightly right of center.

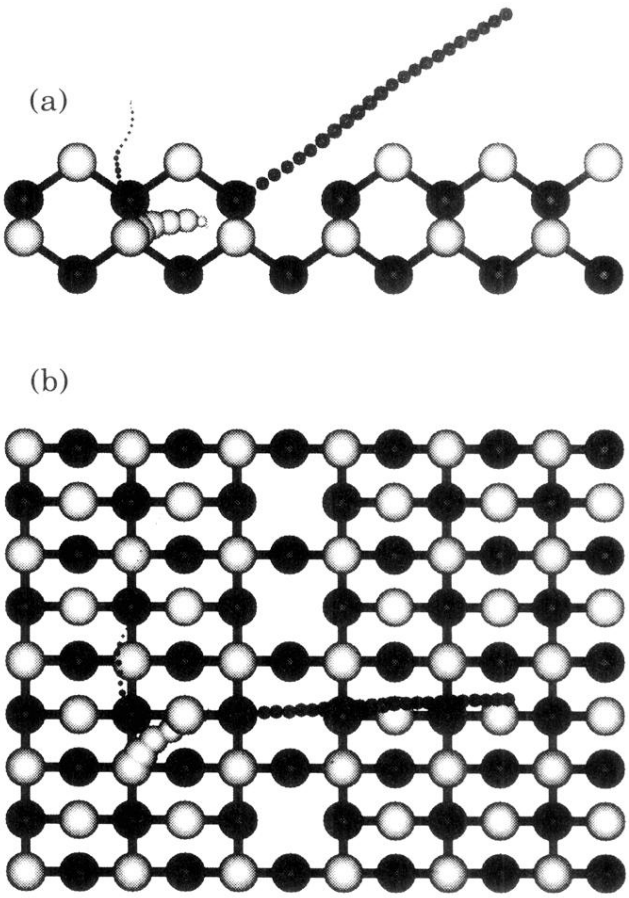

FIG. 11. Time-lapse representation of trajectory leading to ejection of a second-layer atom from the (1×4) surface along the 180° azimuth. See caption to Fig. 7. The atom from the third layer (light sphere) gets deflected by the second-layer atom (dark sphere), and the final momentum transfer is from the deflected third-layer atom to the second-layer atom. A side (upper) and top (lower) view of the same trajectory is presented. The energy of the particle is about 10 eV.

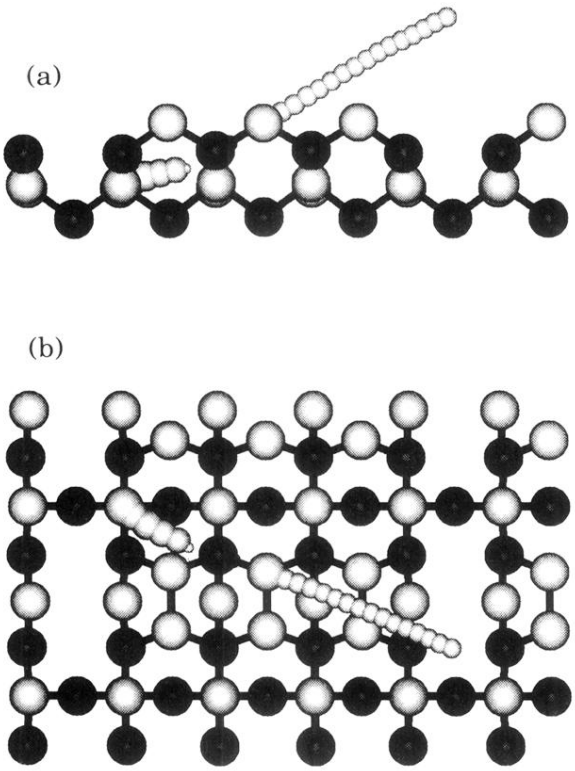

FIG. 12. Time-lapse representation of trajectory leading to ejection of a first-layer atom from the (2×4) reconstruction along the 180°+23° azimuth. See caption to Fig. 7. The atom from the third layer (light sphere) hits the atom from the second layer (dark sphere), and the final momentum transfer from the second-layer atom to the first-layer atom is very fast along the bond axis. A side (upper) and top (lower) view of the same trajectory is presented.

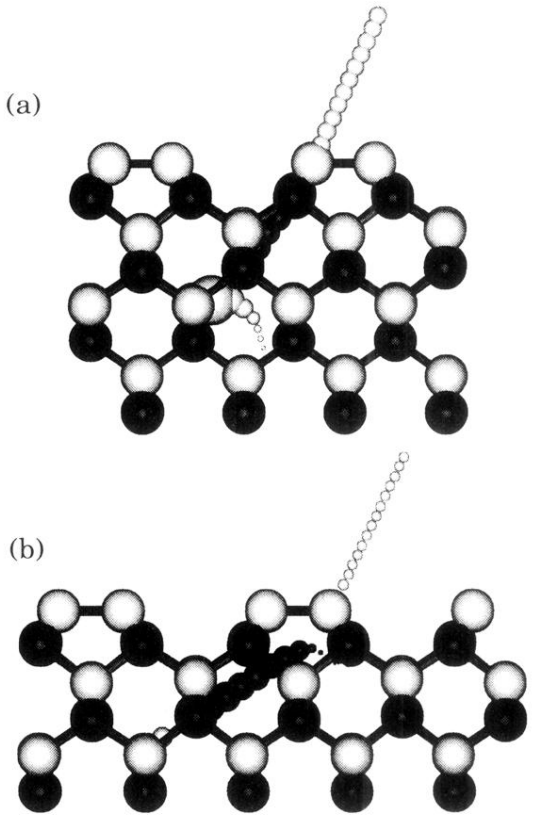

FIG. 13. Time-lapse representation of trajectories leading to ejection of first-layer atoms from the (2×4) reconstruction along the 90° azimuth. See caption to Fig. 7. The atom from the fifth layer (light sphere) hits the atom from the fourth layer (dark sphere), and the final momentum transfer is from the fourth-layer atom to the first-layer atom.

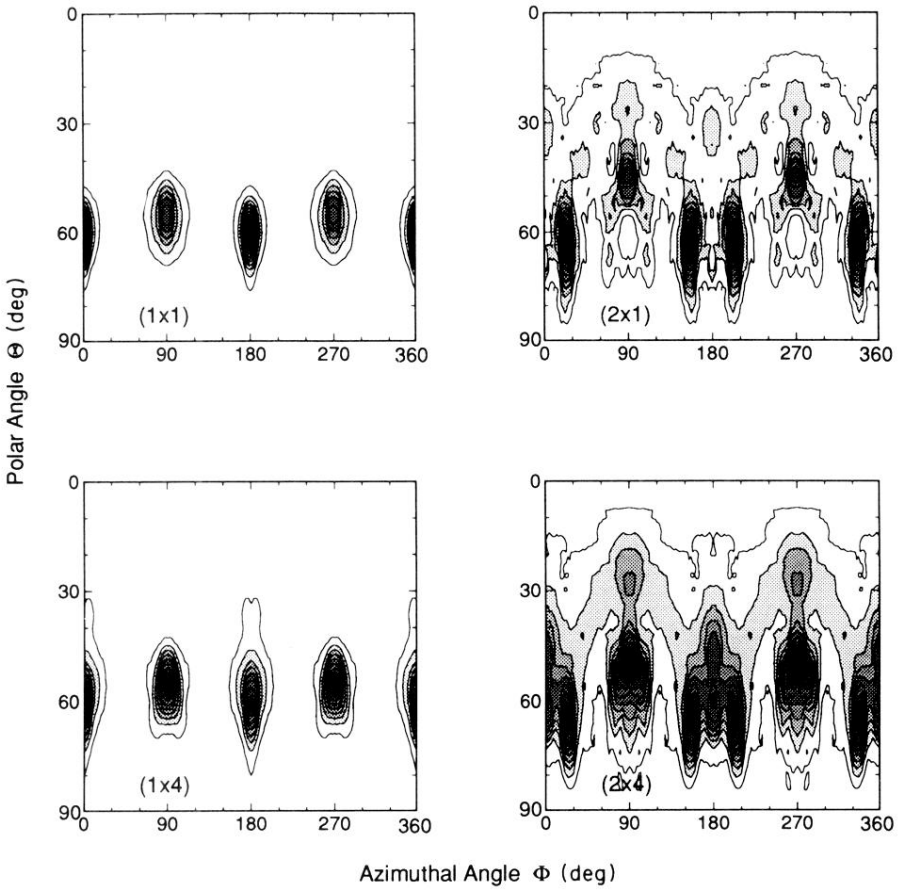

FIG. 3. Final polar-azimuthal-angle distributions of ejected crystal atoms. These distributions include all atoms ejected with energies in the range 5–50 eV. The maximum intensity in each plot has been normalized to unity. The contour values begin at 0.1 and are spaced 0.1 units apart, with areas of darker shading corresponding to higher intensity. The intensities are collected as described in the text and then multiplied by $\sin(\Theta)$ to convert to probability density.

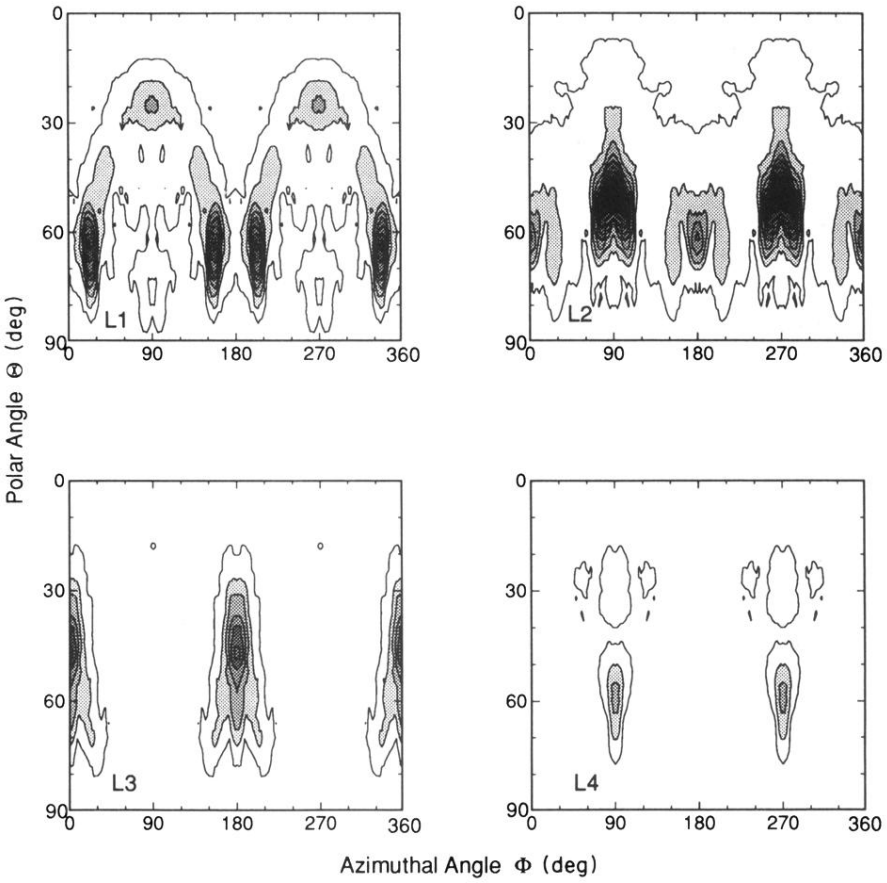

FIG. 5. Layer-resolved, final polar-azimuthal-angle distributions of atoms ejected from the (2×4) surface. These distributions include all atoms ejected with energies in the range 5–50 eV. The distributions for all layers were subject to the same normalization and are directly comparable. The contour values begin at 4 and are spaced two units apart, with areas of darker shading corresponding to higher intensity. The intensities are collected as described in the text and then multiplied by $\sin(\Theta)$ to convert to probability density.

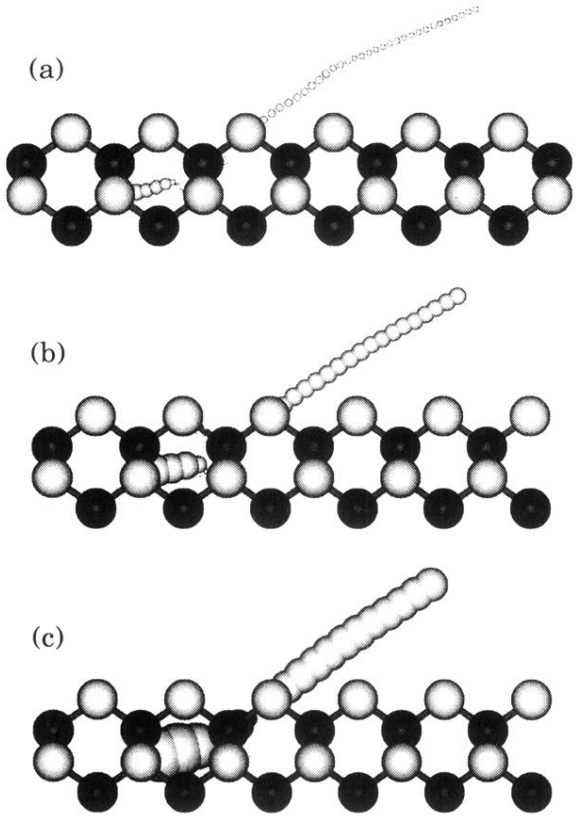

FIG. 7. Time-lapse representation of trajectories leading to ejection of first-layer atoms from the (1×1) surface along the 180° azimuth. Only the motion of the last three atoms in the collision sequence is shown. Sizes of the moving atoms reflect their instantaneous total (kinetic+potential) energy and their positions are plotted at 5-fs intervals. The size of the rigid crystal atoms is equivalent to a 40-eV total energy. The atom from the third layer (light sphere) hits the atom from the second layer (dark sphere), and the final momentum transfer from the second-layer atom to the first-layer atom along the bond axis is very fast. The view angle is parallel to the $\langle 110 \rangle$ or 180° azimuth. The final kinetic energy of the ejected particle is about (a) 5, (b) 20, and (c) 35 eV.

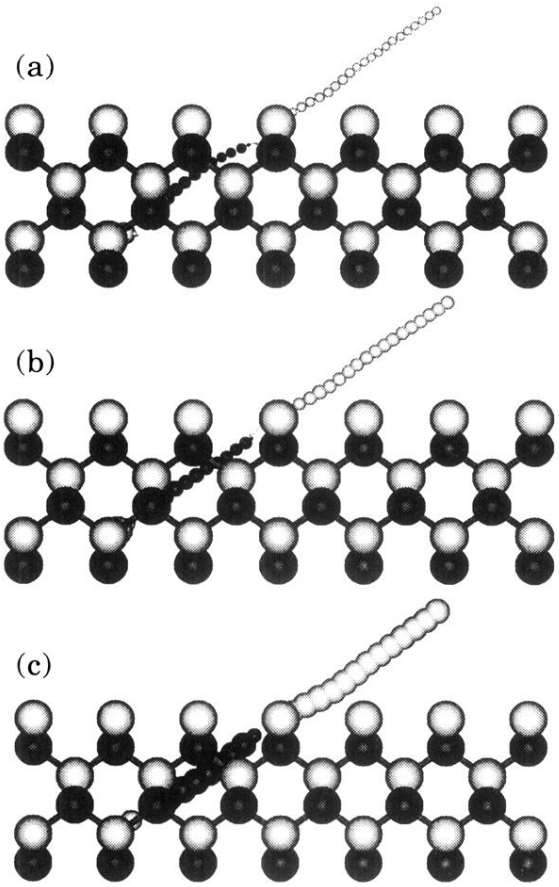

FIG. 8. Time-lapse representation of trajectories leading to ejection of first-layer atoms from the (1×1) surface along the 90° azimuth. See caption to Fig. 7. The atom from the fifth layer (light sphere) hits the atom from the fourth layer (dark sphere), and the final momentum transfer is from the fourth-layer atom to the first-layer atom. The view angle is parallel to the $\langle 1\bar{1}0\rangle$ or 90° azimuth.